ACS APPLIED MATERIALS & INTERFACES

RESEARCH ARTICLE

www.acsami.org

One-Step Electrochemical Synthesis of PtNi Nanoparticle-Graphene Nanocomposites for Nonenzymatic Amperometric Glucose Detection

Hongcai Gao, Fei Xiao, Chi Bun Ching,* and Hongwei Duan*

School of Chemical and Biomedical Engineering, Nanyang Technological University, 70 Nanyang Drive, Singapore 637457

Supporting Information

ABSTRACT: We report a facile one-step ultrasonication-assisted electrochemical method to synthesize nanocomposites of graphene and PtNi alloy nanoparticles (NPs) and their uses for highly selective nonenzymatic glucose detection. We have demonstrated that the obtained nanocomposites exhibit a collection of unique features including well-dispersed NPs with alloy features, high NP loading, and effective reduction of graphene oxide (GO). And the resulting nanoelectrocatalyst shows significantly improved electrochemical performance in nonenzymatic amperometric glucose detection, compared to a number of control electrode materials including the PtNi NP-chemically reduced GO nanocomposites fabricated in two steps (chemical reduction of GO followed by the electrodeposition of metal NPs). Under the physiological condition, the response current of the sensor is linear to glucose concentration up to 35 mM with a sensitivity of 20.42 μA cm^{-2} mM^{-1} at a substantially negative potential (i.e., −0.35 V). Operation under this potential eliminates the impact from the oxidation of common interfering species. This sensor with excellent sensitivity and selectivity also allows for reproducible detection of glucose in human urine samples.

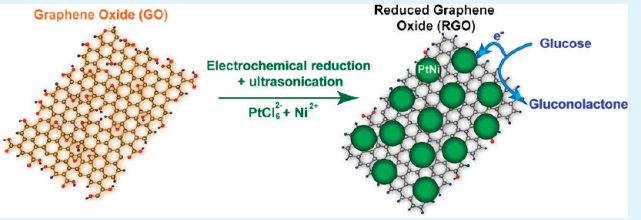

KEYWORDS: electrochemical reduction, graphene, Pt-based alloy nanoparticles, electrocatalysis, glucose, nonenzymatic sensor

INTRODUCTION

Graphene is emerging as a new type of supporting substrates for functional nanomaterials because of a host of intriguing properties such as large surface areas, high electrical conductivity, flexibility, and chemical inertness.[1−3] The integration of graphene and nanoparticles (NPs) of diverse chemical composition has been actively explored for applications ranging from electrocatalysis, photocatalysis to energy harvesting and storage.[4−7] Loading of metal NPs on highly conductive graphene nanosheets gives rise to nanocomposites with larger active surface areas and improved electron transport, making the nanocomposites ideal materials for the fabrication of electrochemical sensor.[8] Preparation of the nanocomposites is typically a two-step procedure involving the chemical reduction of exfoliated graphene oxide (GO) and the attachment of metal NPs.[9−11] In the existing approaches, a layer of organic linker molecules is commonly used to anchor metal NPs on graphene substrates.[12] Although metal NPs can be loaded on graphene in relatively high density in these processes, the use of the organic molecules to link the two components can slow down the direct electron transfer to some extent and possibly block the available active sites on metal NPs and graphene, leading to reduced catalytic activities. Moreover, the possible contamination of chemically reduced GO (CRGO) by the excessive reagents used in GO reduction is also an underlying factor to affect the electrocatalytic performance of the nanocomposites. Therefore, a straightforward green approach toward the nanocomposites free of chemical reducing agents and organic linkers is highly desirable and practically useful for efficient electrocatalysis.

Here we report for the first time a one-step ultrasonication-assisted electrochemical method to synthesize nanocomposites of graphene and PtM (M = Ni and Co) alloy NPs and their uses for highly selective nonenzymatic glucose detection. As illustrated in Figure 1, our results have shown that at a highly negative potential, the simultaneous electrochemical reduction of GO and electrodeposition of alloy NPs led to nanocomposites with dense loading of NPs evenly distributed on the electrochemically reduced GO (ERGO) support. Electrodeposition is a kinetic-controlled process involving preferential nucleation and subsequent growth of NPs on an appropriate electrode surface. The formation of nuclei of nanostructures strongly depends on the interaction between the electrodeposited metal with the substrate (of which the electrode is built). The abundant surface functional groups (−OH, C−O−C, and −COOH) on GO can provide reactive sites for the nucleation and binding of noble metal NPs.[10,11] One major finding is that ultrasonication during the electrodeposition can prevent agglomeration of deposited metal NPs and is critical for the formation of well-dispersed NPs. It is well-known that the high-intensity ultrasonic irradiation generated from ultrasonic probe or ultrasonic agitation leads to both chemical and physical effects, such as mass-transport enhancement, surface cleaning and radical formation, and thereby significantly minimizes the aggregation and reduces the size of the as-obtained NPs. Ultrasonic-electrodeposition is classified into indirect ultrasonication and direct ultrasonication. In indirect

Received: May 6, 2011
Accepted: July 7, 2011
Published: July 07, 2011

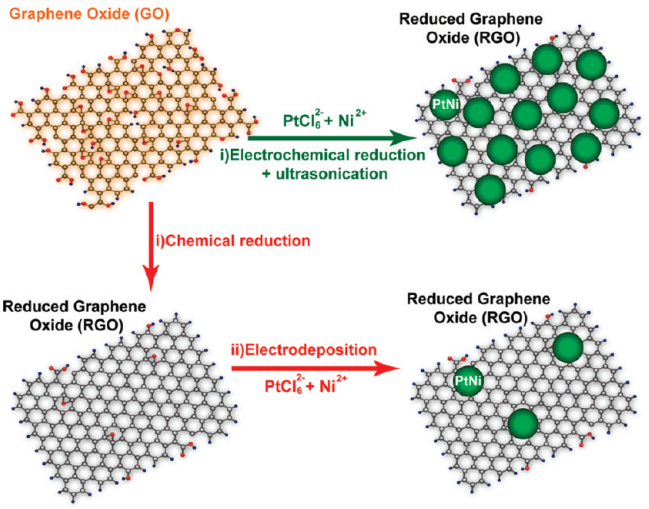

Figure 1. Schematic illustration of the formation of PtNi−RGO nanocomposites by one-step (electrochemical reduction) method and two-step (chemical reduction and electrodeposition) method.

ultrasonic-electrodeposition, the electrolyte solution containing NPs is irradiated by ultrasonic waves before the deposition process to ensure a good dispersion. In direct ultrasonic-electrodeposition, the electrolyte is under continuous ultrasonic irradiation during the electrodeposition. In this work, we use direct ultrasonic-electrodeposition, by which the binding with the active sites and the dispersion of NPs by ultrasonication occur at the same time. In contrast, nanocomposites of PtNi NPs and CRGO fabricated in two steps (chemical reduction of GO followed by the electrodeposition of metal NPs) have shown sparsely loaded NPs (Figure 1) due to the lack of functional binding sites in CRGO. Very recently, one-step reduction of both metal ions precursors and GO has been used to prepare metal NP−CRGO composites; however, these methods were limited to the simultaneous chemical reduction by using reducing agent,[13] sonolysis,[14] and microwave irradiation.[15,16] The one-step electrochemical reduction under ultrasonication in our strategy eliminates the potential contamination in chemical reduction[17−19] and the use of the organic linkers, representing a rapid, efficient, and green approach to fabricate highly active electrocatalysts.

Our choice of glucose as the analyte of interests is motivated by the practical medical needs for diagnosis of human diseases such as diabetes and hyperglycemia.[20] Enzymatic biosensors based on the use of enzymes such as glucose dehydrogenase or glucose oxidase are attractive platforms because of their high sensitivity and excellent selectivity;[21−24] however, the greatest drawback of enzymatic glucose sensors is their insufficient long−term stability originating from their intrinsic dependence on enzyme activity.[25,26] To address this limitation, major research efforts have been devoted to developing nonenzymatic biosensors,[27] such as Pt-based amperometric glucose sensors. Although early research has demonstrated that bulky Pt electrodes suffer from sluggish kinetics to produce significant faradaic currents and severe interferences from electroactive species in body fluids,[27] recent developments have shown that the use of nanostructured Pt electrocatalysts could lead to greatly improved performance in glucose oxidation because of their higher active surface area.[28−32] Meanwhile, increasing evidence has confirmed that Pt-based alloys such as PtPb,[28,33,34] PtIr,[35] and PtRu,[36] exhibit higher catalytic activity and anti-interference ability than pure Pt, generating more stable and larger responses. We have found that our PtNi NPs−ERGO-based electrode shows significantly improved response current toward glucose as well as excellent stability, selectivity and reproducibility, compared to a number of control electrode materials including PtNi NPs−CRGO nanocomposites. This should result from the synergistic contribution of more efficient electrochemical reduction of GO and higher loading of the alloy NPs on ERGO.

EXPERIMENTAL SECTION

Chemicals. Hexachloroplatinate ($H_2PtCl_6 \cdot 6H_2O$, purity: 99.9%), nickel sulfate hexahydrate ($NiSO_4 \cdot 6H_2O$, purity: 99%), cobalt sulfate hexahydrate ($CoSO_4 \cdot 6H_2O$, purity: 99%), graphite powder, and β-D-glucose were obtained from Aldrich. The working solutions were prepared by diluting the stock solution with phosphate buffer solution (PBS) and water. All other chemicals used were of analytical reagent grade.

Instruments. Electrodeposition, electrochemical impedance spectroscopy (EIS), cyclic voltammetric (CV), linear sweep voltammetric (LSV) and chronoamperometric experiments were performed with a CHI 660 D electrochemical workstation (CH Instrument Company, Shanghai, China). A conventional three-electrode system was adopted. The working electrode was a modified glassy carbon electrode (GCE, 3 mm in diameter) or an indium tin oxide (ITO) glass, and the auxiliary and reference electrodes were Pt foil and Ag/AgCl, respectively. The distance between electrodes was kept at 0.5 cm in all experiments. For EIS, the frequency range was 0.1 to 1×10^5 Hz. Atomic force microscopy (AFM) observation was carried out using a MFP3D microscope (Asylum Research) with a silicon cantilever operating in tapping mode. Scanning electron microscope (SEM) image was obtained using JEOL field-emission scanning electron microscope (JSM−6700F), equipped to perform elemental chemical analysis by energy dispersive X-ray spectroscopy (EDX). Fourier transform infrared (FT−IR) spectra were obtained on a Perkin-Elmer Spectrum One Spectrometer. For X-ray photoelectron spectroscopy (XPS) measurements were performed on a Kratos-Axis spectrometer with monochromatic Al Kα (1486.71 eV) X-ray radiation (15 kV and 10 mA) and hemispherical electron energy analyzer. For SEM, EDX, and XPS measurements, the samples were coated on ITO surfaces and measured directly. For IR experiments, the samples were peeled from ITO and collected for the further characterization.

Fabrication of Composite Film-Coated Electrodes. The graphite oxide (GO) was synthesized from graphite powder based on a modified Hummers method.[37] Then the exfoliation of GO was achieved by ultrasonication of the dispersion for 2 h. The CRGO was prepared by adding 35% hydrazine aqueous solution under stirring, and then heated at 95 °C for 1 h.[38] The single-walled carbon nanotubes (SWNT) were purified through refluxing in HNO_3−H_2SO_4 (volume ratio: 1:1) mixture. The GO, CRGO and SWNT were washed with distilled water and dried under vacuum.

Before electrochemical measurement, the GC electrode was polished carefully with 1.0, 0.3, and 0.05 mm alumina powder, respectively, and rinsed with deionized water, followed by sonication in acetone and doubly distilled water successively. Then, the electrode was allowed to dry under nitrogen. Then 10 μL of 0.1 mg L^{-1} pretreated exfoliated GO suspension was transferred on a cleaned GCE, and the solvent was evaporated in air. Thus, a uniform film-coated electrode (i.e., GO/GCE) was obtained. GO/ITO was fabricated by a similar method. The electrochemical reduction of GO/GCE and the electrochemical deposition of PtNi NPs on GO/GCE were performed in 0.2 M Na_2SO_4 aqueous solution containing 0.5 mM H_2PtCl_6 and 50 mM $NiSO_4$. The deposition time was 300 s and the potential was −1.0 V (vs Ag/AgCl). In this case, both GO, Pt and Ni can be reduced completely, hence the

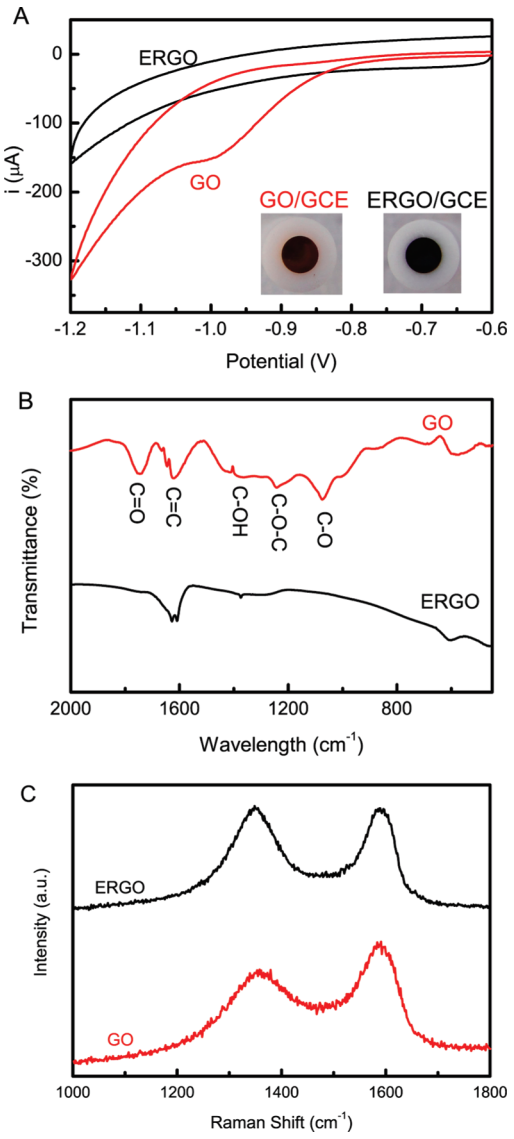

Figure 2. (A) CVs of GO/GCE before and after electrochemical reduction in 0.2 M Na_2SO_4 aqueous solution containing 0.5 mM H_2PtCl_6 and 50 mM $NiSO_4$. Supporting electrolyte: 0.1 M PBS (pH 7.4) saturated with nitrogen gas; Scan rate: 50 mVs^{-1}. The insets are the photos of the GO modified electrode before and after electrochemical reduction. (B) FT−IR transmittance spectra (C) Raman spectra of starting GO and obtained ERGO.

obtained modified electrode is denoted as PtNi−ERGO/GCE. During the potentiostatic deposition, the solution was irradiated with ultrasonic wave.[38,39] The temperature of the solution was maintained at 4.0 ± 0.1 °C using an ice water bath in order to obtain smaller particles. The resulted PtNi−GO/GCE (or ITO) was washed carefully with distilled water and then dried at room temperature. PtNi/GCE, PtNi−CRGO/GCE and PtNi−SWNT/GCE were fabricated through a similar method. Prior to electrochemical deposition, the solution was deoxygenated with nitrogen gas. After each measurement, the potential scan was repeated successively for 10 times in a blank solution for the electrode to regenerate.

RESULTS AND DISCUSSION

Characterization of PtNi−ERGO Nanocomposites. The electrochemical response of a surface is highly sensitive to its physicochemical properties. We investigated the electrochemical behavior of GO modified glass carbon electrode (GO/GCE) before and after electrochemical reduction in metal ion precursor solution by cyclic voltammetric (CV) (Figure 2A). The CV of the starting GO/GCE in a potential range from −0.6 to −1.2 V shows a large cathodic current peak at −0.95 V with a current onset at −0.8 V in phosphate buffer solution (PBS, pH 7.4). This large reduction current is due to the reduction of the surface oxygen groups. After electrodeposited in the metal ions precursor solution containing 0.5 mM H_2PtCl_6 plus 50 mM $NiSO_4$ for 300 s, the PtNi−ERGO/GCE was obtained, and the reduction current at this potential range disappeared. This suggests that the surface-oxygenated species at GO has be completely reduced electrochemically.[17] This is also evidenced by the color change from yellow to black, as shown in the insets of Figure 2A. Fourier transform infrared (FT−IR) spectroscopy was further used to examine the degree of the GO reduction. Figure 2B shows the FT−IR transmittance spectra (KBr) of exfoliated GO and ERGO. The spectrum of GO shows the presence of C−O (ν (epoxy or alkoxy)) at 1065 cm^{-1}, C−O−C (ν (epoxy symmetrical ring deformation vibration)) at 1225 cm^{-1}, C−OH (ν (carboxyl)) at 1400 cm^{-1}, C═C at 1620 cm^{-1}, and C═O in carboxylic acid and carbonyl moieties (ν (carbonyl)) at 1740 cm^{-1}. After electrochemically reduced, the adsorption bands of oxygen functionalities (i.e., C−O at 1065 cm^{-1}, C−O−C at 1225 cm^{-1}, C−OH at 1400 cm^{-1}, and C═O at 1740 cm^{-1}) disappear, only the peak of C═C at 1620 cm^{-1} remains, which confirms that high purity of ERGO can be achieved by using the electrochemical approach.[18] Raman measurements were also used to characterize GO and ERGO samples. As shown in Figure 2C, the Raman spectrum of GO displays two prominent peaks at 1355 and 1590 cm^{-1}, which correspond to the well-documented D and G bands, respectively. Although the Raman spectrum of ERGO samples also have both D and G bands at 1355 and 1590 cm^{-1}, the intensity ratio of D/G increased significantly in comparison with that of the GO. This change in the intensity ratio of the D to G bands is attributed to the increased defect concentration present in ERGO relative to that in GO, indicating the successful deoxygenation in ERGO.

Morphologies of GO and the different nanocomposites investigated in this study were characterized by atomic force microscopy (AFM) and scanning electron microscope (SEM). AFM and SEM images (see the Supporting Information, Figure S1) reveal that the GO nanosheets are well exfoliated and dispersed, with a thickness of about 1.0 nm, similar to the previously reported thickness (1−2 nm) of GO nanosheets,[40] indicating that GO was exfoliated into single or very thin layers. The GO film deposited on GCE displays the characteristic wrinkle morphology, as observed in the SEM images (Figure 3A). And the electrochemical reduction in the metal ion precursor solution (0.5 mM H_2PtCl_6 and 50 mM $NiSO_4$) led to the formation of a dense layer of spherical metal NPs deposited on it (Figure 3B). Observation under higher magnification reveals the well-dispersed PtNi NPs on the wrinkly ERGO support (Figure 3C). These NPs exhibit faceted characteristics and their shape are mostly spherical, with a diameter of about 80 nm. Another finding is that these NPs are stable under the ultrasonic condition, and the resulting biosensor based on these NPs exhibit outstanding performance with long-term stability, which to some extent indicates that the metal NPs are immobilized on the surface of GO through stable bonding such as complex interaction, not simple physical adsorption.

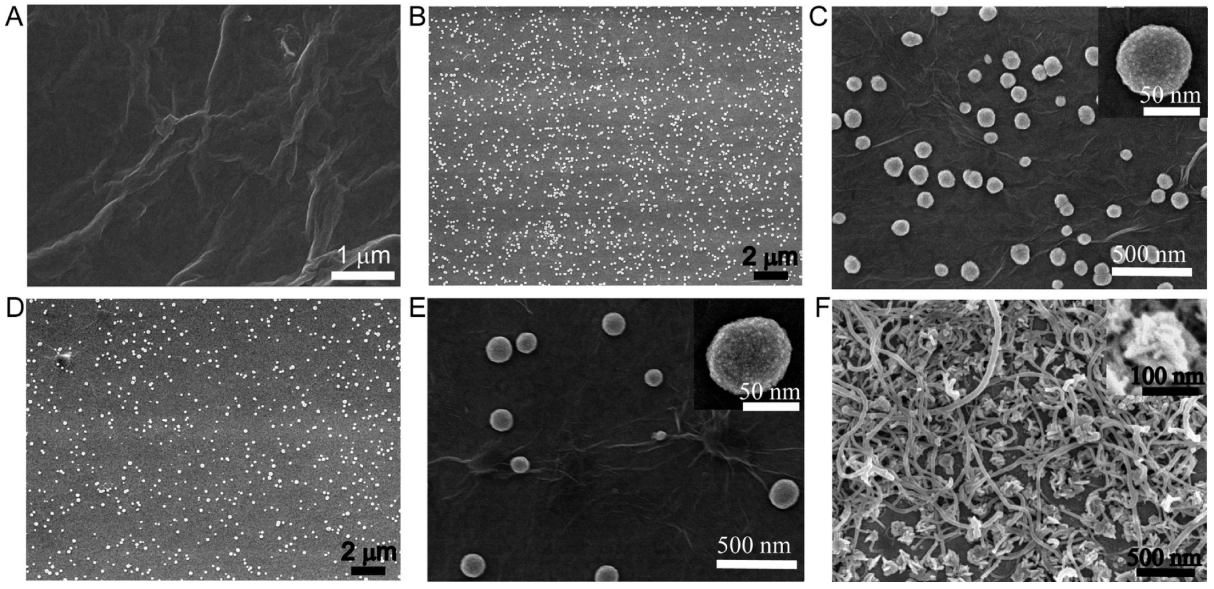

Figure 3. (A) SEM images of as-synthesized GO film; (B) SEM image of PtNi−ERGO nanocompsite, (D) PtNi−CRGO nanocompsite and (F) PtNi−SWNT nanocompsite. (C, E) Magnified SEM images of B and D, respectively.

Moreover, because the applied potential in the electrodeposition is much more negative than the equilibrium (Nernst) potential for the reduction of Pt and Ni, the nuclei form instantly when the potential is applied, and subsequently grow with the time. During the growth stage, the size of loaded metal NPs on the GO surface can be controlled by reaction time in the electrodeposition (see the Supporting Information, Figure S2).

Under the same condition, electrodeposition on CRGO led to sparsely distributed NPs (Figure 3 D). The high surface coverage of metal NPs on ERGO should benefit from the intrinsic surface properties of GO. Surface functional groups such as carboxyl, hydroxyl and carbonyl serve as anchoring sites for the metal NPs. Collectively, NPs of defined sizes were formed on the GO sheets. Whereas for CRGO, most oxygenated species are removed by chemical treatment, resulting in the low affinity of the metal NPs on its surface. Importantly, the highly dispersed and dense metal NPs on supports without any agglomeration usually exhibit a large surface area, which corresponds to higher catalytic activity and sensitivity.

Additionally, it is worthwhile to mention that the polar surface functional groups make GO highly dispersible in aqueous medium. Therefore, both of the GO film deposited from its homogeneous aqueous dispersion and the resulted ERGO film is even and uniform. In contrast, as CRGO restores the sp^2 graphite structure, its dispersity in aqueous medium dramatically decreased and can only form unstable suspension. As a result, the deposited CRGO film exhibited uneven patchy structure (Figure 3 E). This is expected to decrease the performance of the resulted electrode in biosensor and electrocatalysis.

To demonstrate that graphene is a superior carbon support for the electrodeposition of well-defined metal NPs, the PtNi NPs were also deposited on single-walled carbon nanotubes (SWNTs) under the same condition for comparison. In comparison with graphene, SWNTs possess similar stable physical properties but smaller surface areas, which can be considered as rolled graphene. Unlike the uniformly dispersed NPs on graphene surfaces, PtNi NPs are mainly deposited at the tips of the SWNTs and exhibit snowflake-like agglomeration morphology with diameters ranging from 100 to 200 nm (Figure 3F). This difference in NP deposition should be associated with the different spatial distribution of the electrical fields of graphene and SWNTs. For graphene, the electrical field is almost homogeneous along its planar structure, whereas the electrical field of the tips and the sidewalls of the SWNTs are significantly different. Moreover, the distance between the sidewalls of the SWNTs is smaller than the scale of the chronoamperometric diffusion field; $PtCl_6^{2-}$ and Ni^{2+} between the sidewalls of SWNTs are depleted very rapidly in the diffusion-controlled electrochemical reaction, leading to absence of PtNi NPs on the sidewalls and serious aggregation on the tips of the tubes. Aggregation is a serious problem in the development of nanoelectrocatalyst film since it reduces the active surface area.

The formations of GO, CRGO, PtNi−CRGO, and PtNi−ERGO nanocomposite were further characterized by energy dispersive X-ray spectroscopy (EDX) and X-ray photoelectron spectroscopy (XPS). The corresponding EDX spectra of PtNi−ERGO and PtNi−CRGO show the peaks corresponding to C, O, Pt and Ni elements (see the Supporting Information, Figure S3), confirming the existence of bimetallic PtNi NPs on the surface of graphene nanosheets. The atomic ratio of Pt and Ni for PtNi alloy NPs on both ERGO and CRGO are 2/1, and the atomic percentages of Pt and Ni in PtNi−ERGO sample, however, are almost two times those in the PtNi−CRGO sample, demonstrating a higher loading of PtNi NPs on ERGO sheet surface, which is consistent with the SEM observation.

Figures 4A shows the XPS spectra of GO, CRGO, PtNi−ERGO, and PtNi−CRGO nanocomposites, respectively. The peaks centered at the Pt, Ni, C, and O core level regions can be assigned to Pt 4f, Ni 2p, C1s, and O1s, respectively, which further support that bimetallic PtNi NPs have been effectively anchored on the surface of graphene nanosheets. Deconvolution of the Pt 4f signal in both PtNi−ERGO and PtNi−CRGO shows three pairs of doublets (Figures 4B). The most intense doublet with binding energies of 71.8 eV (Pt $4f_{7/2}$) and 75.1 eV (Pt $4f_{5/2}$) is attributed to metallic Pt. Peaks at 72.9 and 76.7 eV could be assigned to Pt^{2+}. The third doublet found at 74.5 and 77.7 eV appears to

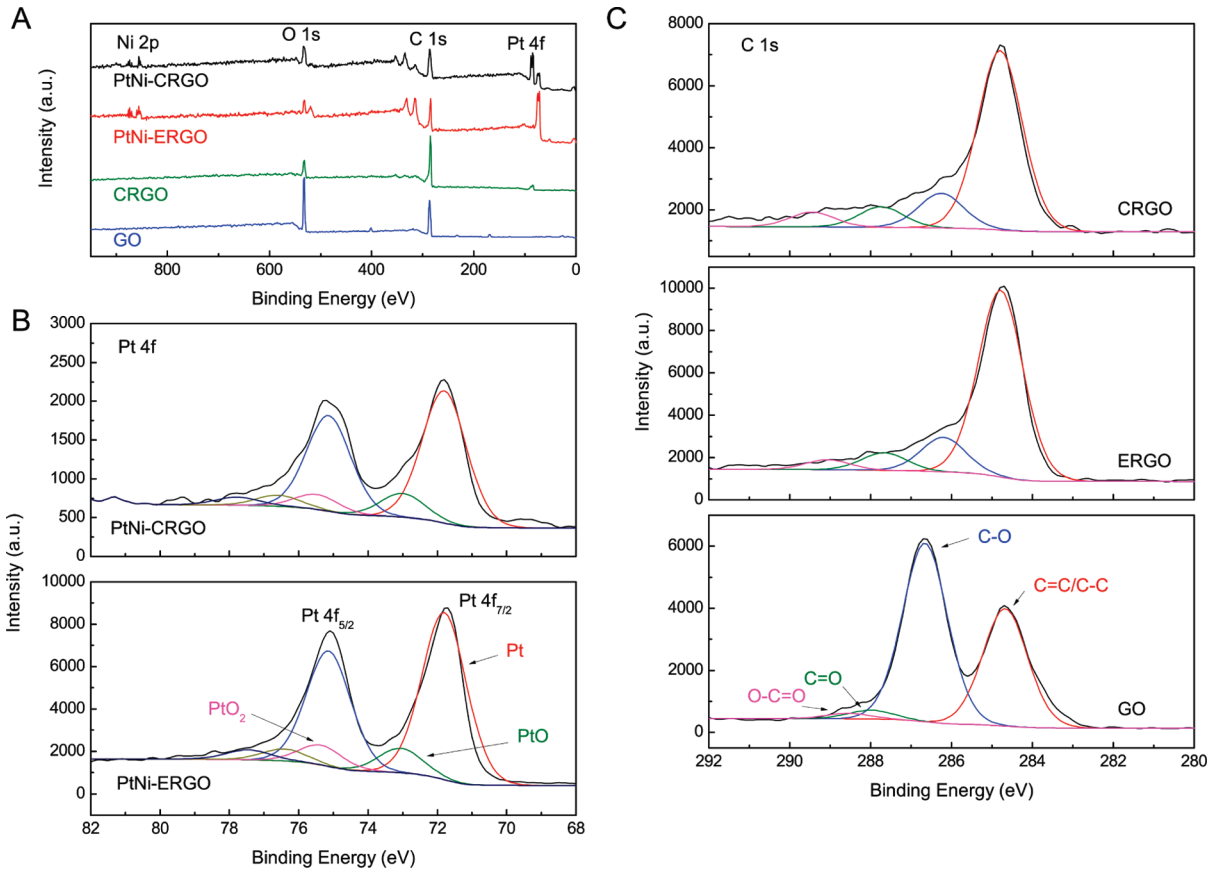

Figure 4. (A) XPS spectra of GO, CRGO, PtNi−ERGO, and PtNi−CRGO nanocomposites; (B) curve fit of Pt 4f spectra of PtNi−ERGO and PtNi−CRGO nanocomposites; (C) curve fit of C 1s spectra of GO, PtNi−ERGO, and CRGO nanocomposites.

be Pt^{4+}. High-resolution XPS scan of the PtNi−ERGO composite shows that the atomic percentage of Pt is ∼10.38%, and the atomic ratio of Pt/Ni is 3/1. For PtNi−CRGO nanocomposite, the atomic percentage of Pt/Ni is similar, but the intensities of XPS peaks in the as-synthesized composites are obviously reduced and the atomic percentage of Pt decreases to ∼2.28%. The decrease in Pt content is consists with the EDX result. There are systematic differences in the alloy compositions obtained from XPS and EDX. This is because EDX characterizes the entire sample, whereas XPS probes a thin surface layer. Taken together, the XPS and EDS data can provide the overall composition of as-prepared alloy NPs.

The curve fit of C 1s spectra of GO, CRGO, and PtNi−ERGO is shown in Figure 4C. The XPS spectrum of GO indicates the presence of two main types of carbon bonds: C═C (284.6 eV) and C═O (286.7 eV). After its electrochemical or chemical reduction, the peaks associated with C═C (284.6 eV) become predominant, whereas the peaks related to the oxidized carbon species are greatly weakened. These results further indicate that GO has been well deoxygenated to form ERGO or CRGO. High-resolution XPS scan of the ERGO composite shows higher atomic percentage of C/O (8/1), in comparison with its precursor GO (2/1) or CRGO (7/1). This indicates the more effective deoxygenation of GO by electrochemical reduction process than chemical reduction, which is very important for improving its conductivity. Therefore, LSV, IR, and XPS collectively demonstrate that GO is successfully reduced to ERGO during the electrodeposition of PtNi NPs.

The conductivity of different composites was tested by the impedance spectroscopy on different electrodes in the presence of equimolar of $[Fe(CN)_6]^{3-/4-}$. These Nyquist plots can be fitted by an equivalent circuit in the inset of Figure 5A, where R_b is bulk resistance of the electrochemical system, R_{ct} is Faradic chargetransfer resistance, and W is the Warburg impedance. Among all the parameters, including R_b (the intersection of the curve at real part Z' in the high frequencies range), R_{ct} (the semicircle at high frequencies), and the Warburg impedance (the slope of the curves at a low frequency), PtNi-ERGO/GCE exhibits remarkably low values of R_b (about 10 Ω), R_{ct} (about 300 Ω calculated by the instrument), and W (as indicated by the precipitous slope at a low frequency), indicating that PtNi-ERGO is an excellent electrode material for electrochemical application. The semicircle of bare GCE is big and the electron transfer resistance is high (R_{ct} = 652 Ω). After modified with exfoliated GO the semicircle dramatically increases (R_{ct} = 926 Ω), suggesting that the exfoliated GO acts as an insulating layer and makes the interfacial charge transfer more difficult. Moreover, the electrostatic repulsion between the negative surface charges of the exfoliated GO and ferricyanide and ferrocyanide ions impairs the access of the ions to the electrode surface for electron communication, also contributing to the increased resistance.[16] When GCE was coated with PtNi−CRGO or PtNi−ERGO nanocomposites, the electron transfer resistance decreased markedly. Two structural factors are responsible for the reduced resistance. First, PtNi alloy NPs have good conductivity and can provide necessary conduction pathways in promoting the

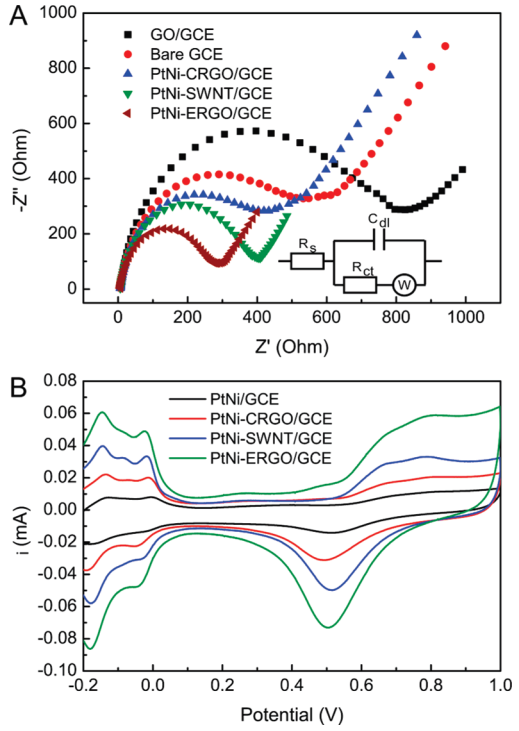

Figure 5. (A) Nyquist plots of GO/GCE, bare GCE, PtNi−CRGO/GCE, PtNi−SWNT/GCE, and PtNi−ERGO/GCE in 0.1 M KCl containing 1.0 mM $K_3Fe(CN)_6$ and 1.0 mM $K_4Fe(CN)_6$. Frequency range: 0.1 to 1×10^5 Hz. The inset is the equivalent circuit. (B) CVs of PtNi/GCE, PtNi−CRGO/GCE, PtNi−SWNT/GCE and PtNi−ERGO/GCE. Supporting electrolyte: 0.5 M H_2SO_4 saturated with nitrogen gas; scan rate: 20 mV s^{-1}.

electron transfer. Second, because of the restoration of a graphitic network sp^2 bonds, electrical conductivity of the ERGO and CRGO films is improved significantly, so the electron transfer between the electrochemical probe $[Fe(CN)_6]^{3-/4-}$ and the electrode is accelerated by ERGO and CRGO.

The CVs of PtNi/GCE, PtNi−CRGO/GCE, PtNi−SWNT/GCE, and PtNi−ERGO/GCE in deaerated 0.5 M H_2SO_4 were collected at a slow potential sweep rate (i.e., 20 mV s^{-1}) and the same potential limit (Figure 5B). The hydrogen adsorption/desorption peaks and the oxide formation/stripping peaks that characterize polycrystalline bulk Pt are readily seen, indicating that Pt-based alloy NPs have been effectively loaded on the supports. No current signal for Ni oxidation or dissolution was observed, suggesting that the particle surface is covered by a Pt-rich layer, and/or that the Ni atoms on the particle surface are stabilized by the neighboring Pt atoms. The cathodic or anodic charge under the parts of the voltammetric curve in the hydrogen adsorption/desorption region permits an estimate of the electrochemically active surface area (S_{EAS}), which can be expressed as: $S_{EAS} = 0.1\ Q_{ads}/Q_{ref}\ L_{Pt}$[41] where Q_{ads} is the integrated hydrogen adsorption charge, Q_{ref} is the hydrogen adsorption charge on a smooth platinum electrode (0.21 mC cm^{-2}) and L_{Pt} is the Pt amount loaded (mg). S_{EAS} values follow the order of PtNi−ERGO/GCE (144.5 $m^2\ g^{-1}$) > PtNi−CNT/GCE (95.86 $m^2\ g^{-1}$) > PtNi−CRGO/GCE (56.30 $m^2\ g^{-1}$) > PtNi/GCE (27.39 $m^2\ g^{-1}$). The largest active surface area of PtNi−ERGO/GCE indicates its promising potentials for electrocatalysis and electrochemical sensor design.

Electrocatalytic Activity toward Glucose Oxidation. Figure 6A presents CVs of a PtNi−ERGO/GCE in a PBS in the absence and presence of 10 mM glucose at a potential scan rate of 10 mV/s. The voltammogram of PtNi−ERGO/GCE in blank PBS is characterized by its well-known hydrogen adsorption/desorption waves at negative potentials, a flat double layer region at intermediate potentials, and Pt oxide formation/reduction waves at positive potentials. In the presence of 10 mM glucose, multiple oxidation peaks were observed during the positive potential sweep. The current peak I at ca. −0.35 V can be attributed to the preferentially electrosorption of glucose on the PtNi bimetallic surface, forming a layer of glucose intermediates (such as the enediol type), which can be easily oxidized. With the potential scanning to a more positive value, the adsorbed glucose intermediates are oxidized on the electrode surface, resulting in the small current peak (peak II at ca. 0.15 V). When the potential further increased, the accumulated intermediates block the surface active sites of the PtNi electrode, which inhibits the electroadsorption of glucose and leads to the sudden drop of current. At potentials go beyond 0.4 V, the adsorbed intermediates are oxidized, forming products such as gluconolactone or gluconic acid (peak III at ca. 0.55 V). At even higher potential, the formation of metal oxide occurs, and the surface becomes less active, causing the current response to decrease again. In the negative scan, the oxidation of glucose is suppressed in the high potential range due to the oxidation of PtNi NPs surfaces. The reduction of surface Pt oxide liberates more surface-active sites for the oxidation of glucose again, resulting in large and broad anodic peaks in the potential range from 0.0 to −0.5 V. These results are in line with the well-accepted mechanism of glucose oxidation on a Pt electrode in neutral media.[28−36]

Figure 6B presents the linear sweep voltammetry (LSV) of the different modified electrodes in a neutral PBS containing 10 mM glucose. No redox peaks can be observed in the CVs of the bare GCE, CRGO/GCE, SWNT/GCE, and ERGO/GCE, suggesting that these electrodes cannot undergo the redox reaction in the potential range of glucose. On PtNi/GCE, PtNi−CRGO/GCE, PtNi−SWNT/GCE, and PtNi−ERGO/GCE, three oxidation peaks are observed during the anodic potential sweep. The glucose oxidation peaks of PtNi−ERGO/GCE are observed at more negative potential, and the current densities are substantially higher than those of PtNi/GCE, PtNi−CRGO/GCE, and PtNi−SWNT/GCE, especially at lower potential, demonstrating that the electrocatalytic oxidation of glucose at the surface of the PtNi−ERGO/GCE is more effective and the electrocatalytic activity of PtNi−ERGO/GCE is much higher than others. This is consistent with the unique spatial distribution of PtNi NPs on the ERGO surface. The high density and well-distributed PtNi NPs would induce more active sites for the catalytic redox reaction and bring about an efficient electrical network through their direct binding with the ERGO. This favorable situation with low transport limitations of substrate would greatly increase the electrocatalytic activity.

Long-term oxidation of glucose on three types of metal (i.e., PtNi, PtCo, and Pt) NPs−ERGO modified electrode was tested via chronoamperometric experiments under the near-peak potential (Figure 6C). As a result, the Pt−ERGO/GCE suffers from serious deactivation, most likely due to poisoning. It is well-known that partially dehydrogenated intermediates act as poisons in electro-oxidation of glucose. The PtNi−ERGO/GCE and PtCo−ERGO/GCE, however, demonstrate a relatively higher current density, and the current density remains steady for a long time. These results reveal that the addition of Co and Ni improves both electrocatalytic activity and stability.

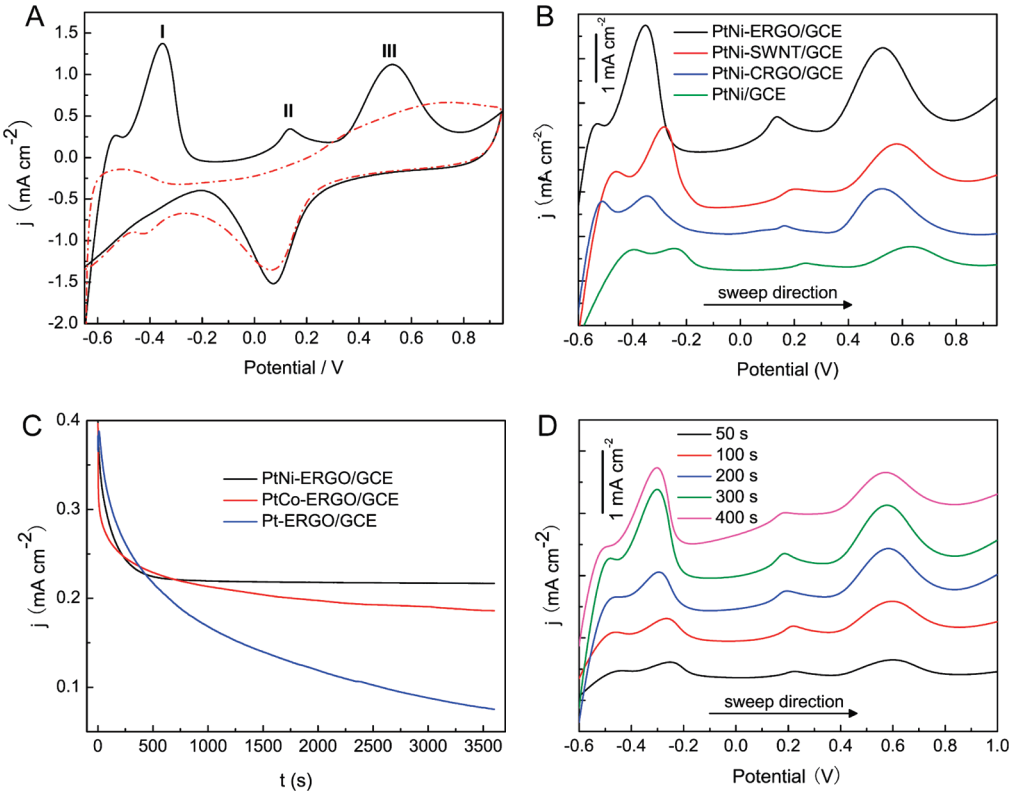

Figure 6. (A) CVs of a PtNi−ERGO/GCE in the absence (red dashed line) and present (black solid line) of 10 mM glucose. (B) LSVs of PtNi/GCE, PtNi−CRGO/GCE, PtNi−SWNT/GCE and PtNi−ERGO/GCE in 10 mM glucose solution. Scan rate: 10 mV s^{-1}. (C) Chronoamperometric curves of PtNi−ERGO/GCE, PtCo−ERGO/GCE, Pt−ERGO/GCE. Applied potential: −0.35 V. (D) LSVs of PtNi-ERGO/GCE at various deposition time of 50, 100, 200, 300, and 400 s in 10 mM glucose solution. Supporting electrolyte: PBS (pH 7.4) saturated with nitrogen gas. Scan rate: 10 mV s^{-1}.

The presence of non-noble metal in the alloy can remove poisonous intermediates and promote electron-transfer reactions owing to their superior catalytic effect to monometallic Pt NPs. The superior catalytic activity of bimetallic systems can be attributed to two effects: One is the "bifunctional effects", which is related to the change of the geometry of the bimetallic systems with respect to the monometallic systems; the other is the "ligand or electronic effect", the role of Co and Ni is a catalytically enhancing agent, which could modify the electronic properties of the Pt.[42] The PtNi−ERGO/GCE shows highest initial current density and limiting current density, therefore, it is chosen for the amperometric measurement of glucose. The LSV responses of PtNi−ERGO/GCE fabricated in the electrodeposition solution with different deposition time to glucose are compared. As shown in Figure 6D, the response current increases with the deposition time changing from 50 to 400 s, with about 40 mV shifts to more negative potential observed. When the deposition time increases beyond 300 s, the response current decreases. This is due to the increase of PtNi alloy NP sizes and the possible reduction of S_{EAS}. The deposition time is hence fixed at 300 s.

Amperometric Measurement of Glucose. The current density-time plots and calibration curve for the sensor under the optimized experimental conditions are depicted in Figure 7A. The sensor responds linearly to glucose up to 35 mM with a detection limit of 0.01 mM (S/N = 3) and detection sensitivity of 20.42 μA cm^{-2} mM^{-1}. These analytical performance parameters are comparable or even superior to those reported in literatures concerning the Pt-based nonenzymatic glucose sensor (see the Supporting Information, Table S1). This linear concentration range is suitable for the determination of glucose level in blood and urine samples.

For sensing applications, electrocatalysts are generally evaluated by measuring current at fixed potential and time after addition of the analyte and possible interfering reagents. Although the normal physiological level of glucose (3.5−6.1 mM) is much higher than that of redox-active interfering species, e.g. ascorbic acid (AA) (0.1 mM) uric acid (UA) (0.02 mM), and AP (0.1 mM), their electron transfer rates are higher than that of glucose. As a result, the oxidation current of them is comparable to that of glucose. Therefore, AA, UA, and AP are major interfering species for the detection of glucose. To avoid the interference, an effective method is to detect glucose at more negative potential. We explored the influence of operating potential on the electro-oxidation of 0.5 mM AA, 0.1 mM UA, 0.1 mM urea, 0.5 mM AAP, 0.5 mM fructose, and 5.0 mM glucose at the PtNi−ERGO/GCE. In the range of −0.35 to 0 V, the oxidation current of glucose is quite prominent, whereas the oxidation currents of AA, UA, urea, and AAP are very small. Furthermore, when the potential was lowered to −0.35 V, the amperometric signals of AA, UA, AP, urea, AAP, and fructose disappeared completely (Figure 7B). Taking into account the sensitivity of the biosensor and interference of easily oxidized compounds presenting in samples, −0.35 V is chosen for the amperometric measurement of glucose in the following experiments.

The influence of other foreign species that may exist in some food and biological samples were also tested, such as urea, fructose, ethanol, glycin, lactamine, serine, aspartic acid, cysteine,

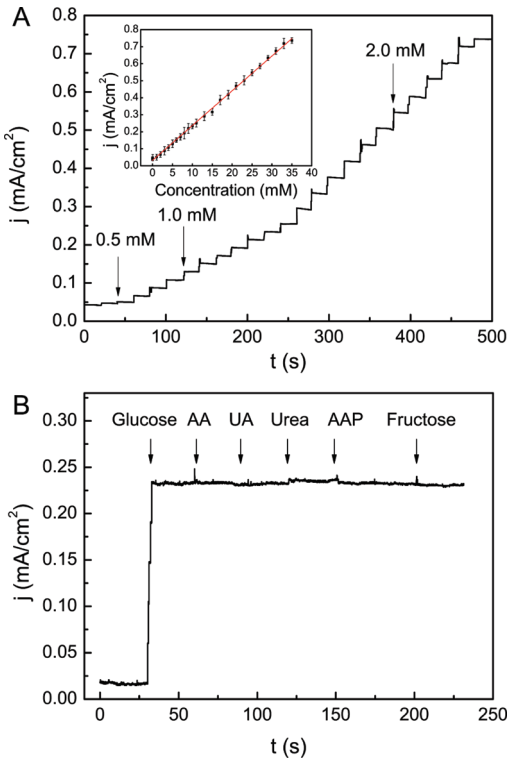

Figure 7. (A) Typical amperometric response of PtNi-ERGO/GCE to successive addition of 0.5, 1.0, and 2.0 mM glucose. And the calibration curve (insert). (B) Influence of electroactive interferences (0.5 mM AA, 0.1 mM UA, 0.1 mM urea, 0.5 mM AAP, and 0.5 mM fructose, from left to right) on the response of 5.0 mM glucose. Supporting electrolyte: 0.1 M PBS (pH 7.4) saturated with nitrogen gas; applied potential: −0.35 V.

xanthine, hypoxanthine, guanine, adenine, thymine, cytosine, Al^{3+}, Fe^{3+}, Fe^{2+}, Ni^{2+}, Co^{2+}, Hg^{2+}, Ca^{2+}, Mg^{2+}, Cd^{2+}, Mn^{2+}, Pb^{2+}, Zn^{2+}, Bi^{2+}, Cl^{-}, SO_4^{2-}, SO_3^{2-}, NO_3^{-}, CO_3^{2-}, and ClO_4^{-}. Our results have shown the foreign species (0.5 or 1.0 mM) led to only minimal changes relative to the response current of 5.0 mM glucose (see the Supporting Information, Table S2), generally less than 5.0%, compared with that recorded in absence of the foreign substance. This means that these substances do not interfere with the determination of glucose, and the obtained sensor possesses high selectivity.

The reproducibility and stability of the sensor are also evaluated. The current response of ten electrodes modified identically to 1.0 mM glucose at −0.35 V displayed a relative standard deviation (RSD) less than 5.0%, confirming that the sensor is highly reproducible. Ten successive measurements using one sensor yielded an RSD of 4.2% (see the Supporting Information, Figure S4), indicative of the stability of the sensor for long-term uses. The stability of PtNi−ERGO/GCE stored at room temperature is investigated by periodically recording its current response to 10.0 mM glucose. The nonenzymatic sensor retained 93.2 and 90.5% of its initial sensitivity at 10 and 50 days postpreparation, respectively (see the Supporting Information, Figure S5).

To illustrate the feasibility of the nanocomposite modified electrode in practical analysis, weused the PtNi− ERGO/GCE to detect glucose in human urine samples. A rapid and stable amperometric response was acquired at −0.35 V with the addition of 9.0 mL of sample into 1.0 mL of PBS. The contents of glucose in urine can be calculated from the established calibration curve. The recovery was ranging from 91.3 to 108.2%, with RSD less than 5% calculated from ten separate experiments (see the Supporting Information, Table S3). The good recoveries indicated that the determination of glucose using PtNi−ERGO/GCE was highly effective.

CONCLUSION

In summary, PtNi alloy NP−graphene composite was developed through a facile and green one-step electrochemical reduction process from GO and metal precursors, by which well-dispersed alloy NPs with high density can be loaded on the effectively electrochemically reduced GO. As compared with PtNi alloy NPs, PtNi−CRGO and PtNi−SWNT nanocomposites, PtNi−ERGO modified electrode exhibits smaller electron transfer resistances and larger electrochemically active surface area, which makes it an ideal electrode material for electrocatalytic application. When used for glucose sensing, we found that the PtNi−ERGO nanocomposite based nonenzymatic sensor possesses many merits in terms of high selectivity, superior resistance to poisoning, low detection limit, rapid response, excellent reproducibility and stability, which outmatches the performance of any other nonenzymatic Pt-based glucose sensor that have been reported (see the Supporting Information for the comparison). The combination of these unique characters has enabled the application of this new type of nanoelectrocatalyst loaded electrodes for real human samples.

ASSOCIATED CONTENT

Supporting Information. Experimental details and supplementary figures and tables (PDF). This material is free of charge via the Internet at http://pubs.acs.org.

AUTHOR INFORMATION

Corresponding Author

*E-mail: hduan@ntu.edu.sg (H.D.); cbching@ntu.edu.sg (C B.C.).

ACKNOWLEDGMENT

H.D. acknowledges the program of Nanyang Assistant Professorship for financial support.

REFERENCES

(1) Park, S.; Ruoff, R. S. *Nat. Nanotechnol.* **2009**, *4*, 217–224.
(2) Matsumoto, Y.; Koinuma, M.; Kim, S. Y.; Watanabe, Y.; Taniguchi, T.; Hatakeyama, K.; Tateishi, H.; Ida, S. *ACS Appl. Mater. Interfaces* **2010**, *2*, 3461–3466.
(3) Kamat, P. V. *J. Phys. Chem. Lett.* **2010**, *1*, 520–527.
(4) Wang, X. L.; Han, W. Q. *ACS Appl. Mater. Interfaces* **2010**, *2*, 3709–3713.
(5) Wu, Z. S.; Ren, W. C.; Wen, L.; Gao, L. B.; Zhao, J. P.; Chen, Z. P.; Zhou, G. M.; Li, F.; Cheng, H. M. *ACS Nano* **2010**, *4*, 3187–3194.
(6) Guo, S. J.; Dong, S. J.; Wang, E. K. *ACS Nano* **2010**, *4*, 547–555.
(7) Fan, G. F.; Zhu, H. W.; Wang, K. L.; Wei, J. Q.; Li, X. M.; Shu, Q. K.; Guo, N.; Wu, D. H. *ACS Appl. Mater. Interfaces* **2011**, *3*, 721–725.
(8) Shan, C. S.; Yang, H. F.; Han, D. X.; Zhang, Q. X.; Ivaska, A.; Niu, L. *Biosens. Bioelectron.* **2010**, *25*, 1070–1074.
(9) Goncalves, G.; Marques, P.; Granadeiro, C. M.; Nogueira, H. I. S.; Singh, M. K.; Gracio, J. *Chem. Mater.* **2009**, *21*, 4796–4802.
(10) Zhang, S.; Shao, Y. Y.; Liao, H. G.; Liu, J.; Aksay, I. A.; Yin, G. P.; Lin, Y. H. *Chem. Mater.* **2011**, *23*, 1079–1081.

(11) Xu, C.; Wang, X.; Zhu, J. W. *J. Phys. Chem. C* **2008**, *112*, 19841–19845.
(12) Li, G. L.; Liu, G.; Li, M.; Wan, D.; Neoh, K. G.; Kang, E. T. *J. Phys. Chem. C* **2010**, *114*, 12742–12748.
(13) Tang, X. Z.; Cao, Z. W.; Zhang, H. B.; Liu, J.; Yu, Z. Z. *Chem. Commun.* **2011**, *47*, 3084–3086.
(14) Vinodgopal, K.; Neppolian, B.; Lightcap, I. V.; Grieser, F.; Ashokkumar, M.; Kamat, P. V. *J. Phys. Chem. Lett.* **2010**, *1*, 1987–1993.
(15) Guo, S. J.; Wen, D.; Zhai, Y. M.; Dong, S. J.; Wang, E. K. *ACS Nano* **2010**, *4*, 3959–3968.
(16) Jasuja, K.; Linn, J.; Melton, S.; Berry, V. *J. Phys. Chem. Lett.* **2010**, *1*, 1853–1860.
(17) Shao, Y. Y.; Wang, J.; Engelhard, M.; Wang, C. M.; Lin, Y. H. *J. Mater. Chem.* **2010**, *20*, 743–748.
(18) Guo, H. L.; Wang, X. F.; Qian, Q. Y.; Wang, F. B.; Xia, X. H. *ACS Nano* **2009**, *3*, 2653–2659.
(19) Zhou, M.; Wang, Y. L.; Zhai, Y. M.; Zhai, J. F.; Ren, W.; Wang, F. A.; Dong, S. J. *Chem.—Eur. J.* **2009**, *15*, 6116–6120.
(20) Wan, D.; Yuan, S. J.; Li, G. L.; Neoh, K. G.; Kang, E. T. *ACS Appl. Mater. Interfaces* **2010**, *2*, 3083–3091.
(21) Yehezkeli, O.; Tel-Vered, R.; Reichlin, S.; Willner, I. *ACS Nano* **2011**, *5*, 2385–2391.
(22) Uehara, H.; Kakiage, M.; Sekiya, M.; Sakuma, D.; Yamonobe, T.; Takano, N.; Barraud, A.; Meurville, E.; Ryser, P. *ACS Nano* **2009**, *3*, 924–932.
(23) Zhang, Z. B.; Yuan, S. J.; Zhu, X. L.; Neoh, K. G.; Kang, E. T. *Biosens. Bioelectron.* **2010**, *25*, 1102–1108.
(24) Lu, J.; Do, I.; Drzal, L. T.; Worden, R. M.; Lee, I. *ACS Nano* **2008**, *2*, 1825–1832.
(25) Cheng, T. M.; Huang, T. K.; Lin, H. K.; Tung, S. P.; Chen, Y. L.; Lee, C. Y.; Chiu, H. T. *ACS Appl. Mater. Interfaces* **2010**, *2*, 2773–2780.
(26) Fang, B.; Gu, A. X.; Wang, G. F.; Wang, W.; Feng, Y. H.; Zhang, C. H.; Zhang, X. J. *ACS Appl. Mater. Interfaces* **2009**, *1*, 2829–2834.
(27) Jena, B, K.; Raj, C. R. *Chem.—Eur. J.* **2006**, *12*, 2702–2708.
(28) Wang, J.; Thomas, D. F.; Chen, A. *Anal. Chem.* **2008**, *80*, 997–1004.
(29) Park, S.; Chung, T. D.; Kim, H. C. *Anal. Chem.* **2003**, *75*, 3046–3049.
(30) Song, Y. Y.; Zhang, D.; Gao, W.; Xia, X. H. *Chem.—Eur. J.* **2005**, *11*, 2177–2182.
(31) Yuan, J. H.; Wang, K.; Xia, X. H. *Adv. Funct. Mater.* **2005**, *15*, 803–809.
(32) Shen, Q. M.; Jiang, L. P.; Zhang, H.; Min, Q. H.; Hou, W. H.; Zhu, J. J. *J. Phys. Chem. C* **2008**, *112*, 16385–16392.
(33) Cui, H. F.; Ye, J. S.; Zhang, W. D.; Li, C. M.; Luong, J. H. T.; Sheu, F. S. *Anal. Chim. Acta* **2007**, *594*, 175–183.
(34) Bai, Y.; Sun, Y. Y.; Sun, C. Q. *Biosens. Bioelectron.* **2008**, *24*, 579–585.
(35) Holt-Hindle, P.; Nigro, S.; Asmussen, M.; Chen, A. C. *Electrochem. Commun.* **2008**, *10*, 1438–1441.
(36) Xiao, F.; Zhao, F. Q.; Mei, D. P.; Mo, Z. R.; Zeng, B. Z. *Biosens. Bioelectron.* **2009**, *24*, 3481–3486.
(37) Hummers, W. S.; Offeman, R. E. *J. Am. Chem. Soc.* **1958**, *80*, 1339–1339.
(38) Li, D.; Muller, M. B.; Gilje, S.; Kaner, R. B.; Wallace, G. G. *Nat. Nanotechnol.* **2008**, *3*, 101–105.
(39) Xiao, F.; Zhao, F. Q.; Zhang, Y. F.; Guo, G. P.; Zeng, B. Z. *J. Phys. Chem. C* **2009**, *113*, 849–855.
(40) Novoselov, K. S.; Geim, A. K.; Morozov, S. V.; Jiang, D.; Zhang, Y.; Dubonos, S. V.; Grigorieva, I. V.; Firsov, A. A. *Science* **2004**, *306*, 666–669.
(41) Radmilovic, V.; Gasteiger, H. A.; Ross, P. N. *J. Catal.* **1995**, *154*, 98–106.
(42) Babu, P. K.; Kim, H. S.; Oldfield, E.; Wieckowski, A. *J. Phys. Chem. B* **2003**, *107*, 7595–7600.